JACS
JOURNAL OF THE AMERICAN CHEMICAL SOCIETY

ARTICLE

pubs.acs.org/JACS

Conformation-Changing Aggregation in Hydroxyacetone: A Combined Low-Temperature FTIR, Jet, and Crystallographic Study

Archna Sharma,*[,†] Igor Reva,[†] Rui Fausto,[†] Susanne Hesse,[‡] Zhifeng Xue,[‡] Martin A. Suhm,[‡] Susanta K. Nayak,[§] Ranganthan Sathishkumar,[§] Rumpa Pal,[§] and Tayur N. Guru Row[§]

[†]Department of Chemistry, University of Coimbra, Coimbra, Rua Larga 3004-535, Portugal

[‡]Institut für Physikalische Chemie, Universität Göttingen, Tammannstrasse 6, D-37077 Göttingen, Germany

[§]Solid State and Structural Chemistry Unit, Indian Institute of Science, Bangalore-560012, India

Supporting Information

ABSTRACT: Aggregation in hydroxyacetone (HA) is studied using low-temperature FTIR, supersonic jet expansion, and X-ray crystallographic (in situ cryocrystallization) techniques. Along with quantum chemical methods (MP2 and DFT), the experiments unravel the conformational preferences of HA upon aggregation to dimers and oligomers. The O−H···O=C intramolecular hydrogen bond present in the gas-phase monomer partially opens upon aggregation in supersonic expansions, giving rise to intermolecular cooperatively enhanced O−H···O−H hydrogen bonds in competition with isolated O−H···O=C hydrogen bonds. On the other hand, low-temperature IR studies on the neat solid and X-ray crystallographic data reveal that HA undergoes profound conformational changes upon crystallization, with the HOCC dihedral angle changing from ∼0° in the gas phase to ∼180° in the crystalline phase, hence giving rise to a completely new conformation. These conclusions are supported by theoretical calculations performed on the geometry derived from the crystalline phase.

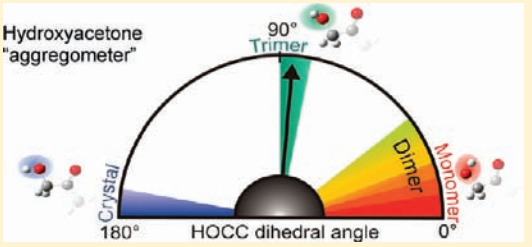

INTRODUCTION

Intermolecular interactions may induce conformational changes upon aggregation of gas-phase molecules to oligomers. Hydrogen-bonded systems are of particular interest in this regard, as the formation of intermolecular hydrogen-bonded networks upon aggregation may compete with existing intramolecular hydrogen bonds, giving rise to conformational changes. Several studies on this topic have been reported, particularly on carbohydrates such as glycolaldehyde, dihydroxyacetone, etc., on account of their multiple hydrogen-bond contacts[1−3] and their ability to undergo conformational changes under different experimental conditions. Also, molecular self-recognition of chiral α-hydroxy esters in the gas phase has been reported,[4−6] involving a subtle interplay between different hydrogen-bond contacts among hydroxyl and carbonyl groups.

Because of its astrophysical and industrial significance, hydroxyacetone (HA) has been the subject of various experimental and theoretical studies.[7−11] Several spectroscopic methods have been applied to study the compound under various experimental conditions, for example, gas phase, neat solid state, solution, and isolated in low-temperature inert matrices.[7,9,12] Some of us have recently reported a detailed IR spectroscopic analysis of HA isolated in an argon matrix,[12] which was complemented by a deep analysis of conformational isomerism of the HA monomer by up-to-date theoretical methods (MP2//DFT/6-311++G(d,p)). In that study, out of four predicted different minima, only two were found to be stable conformers (Cc and Tt, Figure 1), while for the remaining structures the zero-point energy levels were found to be above the barriers separating them from Cc or Tt. The most stable Cc form is characterized by possessing a strained intramolecular hydrogen bond (O−H···O angle being 117.4° in DFT and 118.4° in MP2 approximation) and was the only monomeric form observed experimentally in that study.[12] The calculated gas-phase Boltzmann population was Cc:Tt = 99:1, while in the polarized continuum model[13,14] for the dielectric constant of water, a third conformation Ct (Figure 1) also contributed. In this calculation, the Cc:Ct:Tt ratio was predicted to be 83:11:6. Existence of an additional conformer (Ct) in water solution[12] provided a further clue on the dependence of conformational isomerism in HA upon the environment. Surely, explicit hydrogen bonding in the first hydration sphere would also be important in real water. A comparison of the theoretical spectra of these three conformers with the experimental IR spectrum reported by Mohaček-Grošev[11] agreed that open forms should be present in aqueous solution of HA. Together with the results of an experimental study conducted on the gas and particulate (with mean particle size ∼50 nm) phases of HA,[7] this provided evidence about a partial breakup of the intramolecular hydrogen bond in the Cc conformer upon aggregation. According to these studies, HA nanometer to micrometer particles consist predominantly of the open forms of the molecule where the hydroxyl

Received: April 14, 2011
Published: September 30, 2011

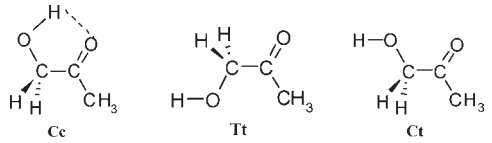

Figure 1. HA conformers, found to exist in cryogenic matrices (Cc and Tt), and an additional conformer (Ct) found to exist in water solution.

group takes part in intermolecular hydrogen bonding. The authors, however, did not report the structure of the predicted conformer.

Supersonic jet expansions have been used to enforce aggregation by rapid cooling in other α-hydroxy carbonyl compounds.[4−6] Upon expansion, these molecules were seen to form complexes including a change in conformation of the monomeric forms. In most of the cases, the changes were accompanied again by the partial or full break-up of the intramolecular hydrogen bonds present in these systems. Frequently, the structural conclusions required the comparison of IR and Raman jet techniques.[15,16]

It would thus be interesting to get a detailed insight into the conformational effect of HA aggregation combining supersonic jet expansion, low-temperature cryogenic spectroscopy, and X-ray crystallography (in situ cryocrystallization). We started our study by investigating small aggregates, which could be prepared using supersonic expansions and probed by IR and Raman techniques. We then proceeded toward the study of larger aggregates in the condensed phase. Because low-temperature FTIR spectroscopy allows for the identification of structural motifs of compounds in their glassy and crystalline states,[17−19] this technique was used in the present case also for the characterization of solid-state conformers of HA. To obtain a complete structural picture, diffraction techniques are desirable. X-ray diffraction is commonly used to investigate interactions between hydrogen-bond donors and acceptors and helps in establishing the type and extent of hydrogen bonding in solids.[20,21] It may be mentioned that neutron diffraction would be the ideal choice to locate and refine the positions of hydrogen atoms; however, the requirement of large sized crystals is a serious limiting step. In situ cryocrystallization of liquids has been used effectively, over the years, in the determination of their molecular and crystal structures and in the study of prevalent intermolecular interactions.[22−26] The same approach was used in the present case also, to probe the structural details of solid HA that were unlikely to be found by other techniques. Finally, theoretical methods were used to provide support to the experimental findings.

EXPERIMENTAL DETAILS

Low-Temperature Neat Solid Film. HA was obtained from Aldrich (Acetol, Tech., 90%) and was further purified by repeated freeze−pump−thaw procedures. The experimental setup is only described briefly. For a detailed description, please see ref 12. For the experiments carried out in the neat solid state, the compound was deposited onto the CsI window of the cryostat (APD Cryogenics closed-cycle helium refrigerator with DE-202A expander) kept at a temperature of 12 or 175 K. The temperature was controlled within 1 K using a Scientific Instruments digital temperature controller with a silicon diode sensor (model 9659). Details of the input system used in the deposition are given elsewhere.[12] The valve nozzle, used to deposit the sample, was kept at room temperature (~25 °C). IR spectra were recorded using a Mattson (60 AR, Infinity series) FTIR spectrometer equipped with a KBr beamsplitter and a deuterated triglycine sulfate detector (DTGS), with 0.5 cm^{-1} resolution.

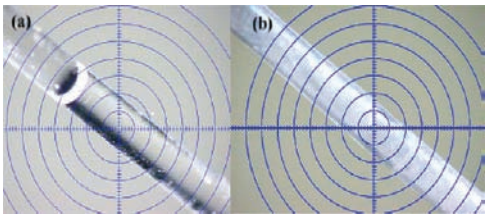

Figure 2. (a) Liquid mounted and (b) single crystal in the Lindemann capillary on diffractometer.

Jet FTIR Spectra. In the jet FTIR experiment, the expansion from a slit nozzle with a length of 600 mm and a width of 0.2 mm was probed in direct absorption by a focused FTIR beam with an average diameter of 15 mm (Bruker IFS 66v/S). Reference spectra without expansion were collected immediately before the gas pulse. The buildup of background pressure in the pulsed jet experiments was limited by a 23 m^3 stainless steel vacuum chamber followed by a pumping system and by up to 40 s pumping intervals between pulses. Typically, data from 50 gas pulses were coadded for the IR spectra shown in this work. Gas pulses (~140 ms duration) were controlled by magnetic valves. Liquid HA was deposited on a sintered glass filter and seeded into the carrier gas (He 99.996% or Ar 99.998%) by flowing the gas at 1−2 bar through this filter. Concentrations were roughly estimated on the basis of gas-phase spectra and theoretical band strengths. Rotational temperatures of monomers and clusters drop to 10−30 K, whereas effective conformational temperatures are typically higher due to interconversion barriers.[16] The FTIR signal was detected by a large area InSb detector (spectral range 3700−3100 cm^{-1}) or MCT detector (spectral range 1900−1000 cm^{-1}) equipped with an appropriate optical filter. The spectral resolution was 2 cm^{-1}.

Jet Raman Spectra. Similar to the IR jet studies, He (Linde, 99.996%), Ne (Linde, 30% in He), and Ar (Linde, 99.999%) were flowed either in pure or in premixed form at ~1.5 bar through a thermostatted glass saturator, in which HA was cooled to 15 or 10 °C. To identify spectral features involving water impurities, a higher purity HA sample (ABCR, 95%) was also used. The gas mixture was collected in a 4.7 L Teflon-coated reservoir and expanded through a home-built 4.0 × 0.15 mm^2 slit nozzle into the chamber evacuated by a series of pumps. The stagnation pressure in the reservoir (100−700 mbar) and the distance (1, 2 mm) from the continuous 18 W 532 nm laser to the nozzle exit were varied to influence the ratio of the different clusters/conformers. The Raman scattering was collected at a 90° angle, dispersed in a monochromator after filtering out the Rayleigh contribution, and detected by a back-illuminated liquid-N_2-cooled CCD camera. The spectra represent averages over three to four 300 s jet measurements and the cosmic ray signals were removed iteratively by comparing these measurement blocks. Measurements in a vacuum under otherwise identical conditions were used as reference spectra. Calibration with Ne lines yielded the spectra displayed in the Results and Discussion. Concentrations are extrapolated from published vapor pressures at different temperatures and are in line with the jet FTIR values under comparable experimental conditions. Rotational and conformational temperatures are somewhat higher than in the IR case due to the short nozzle distance.[15]

X-ray Crystallography. Hydroxyacetone was filled in a Lindemann capillary of 0.3 mm diameter, and the capillary was cut to size (~2.5 cm long) to fit on the goniometer and sealed at both ends. In situ cryocrystallography experiments were performed on a Bruker AXS X-ray diffractometer equipped with SMART APEX CCD area detector. Cryocooling was achieved using an OXFORD N_2 cryosystem (Figure 2a). The liquid was cooled at a ramp rate of 45 K h^{-1} to 90 K. Uniformity in the temperature on the capillary was maintained by continuous rotation

of the sample. The solidified sample was annealed by physically shifting the nitrogen stream back and forth from the capillary until a single crystal was obtained. Initially, the crystal was not formed during the cooling cycle; however, the compound crystallized during the heating cycle at 110 K, while heating from 90 K. The quality of the single crystal formed (Figure 2b) was monitored by taking both still and rotation photographs. To check the possibility of formation of other polymorphic forms based on both kinetic and thermodynamic stability,[22] different ramp rates (30, 50, 100, 120 K h^{-1}) in the cooling and heating cycles were employed. In all cases, the same crystalline form appears to have formed. Once a good quality crystal was obtained by following the above procedure, a rotation photograph was taken prior to data collection to ascertain the quality of the diffraction spots. The temperature was allowed to stabilize for half an hour at the intended data collection temperature of 110 K, after which 180 frames of data were collected with 2θ fixed at $-25°$ and a ω scan width of $-1°$. The frames were then processed using SMART,[27] and the spots were analyzed using RLATT[27] to determine the unit cell dimensions. The indexed reflections correspond to the orthorhombic system. Data were collected on four sets of 606 frames with $2\theta = -25°$ and with ϕ values of 0°, 90°, 180°, and 270°, respectively. The crystal structure was solved using SIR92[28] and refined using the program package SHELXL[29] from the program suite WinGX.[30] The molecular diagrams were generated using ORTEP-3,[31,32] and packing diagrams were generated using Mercury.[33] All of the geometric calculations were carried out by PARST95[34] and PLATON.[35] All non-hydrogen atoms were refined anisotropically, and the hydrogen atoms located from difference Fourier maps were refined isotropically.

COMPUTATIONAL METHODS

Quantum chemical calculations on dimers and oligomers were performed with the Gaussian 03 suite of programs[36] at the DFT(B3LYP)[37−39] and MP2[40] levels of theory, using the 6-31G(d,p),[41] 6-311+G(d) and 6-311++G(d,p),[42] and aug-cc-pVTZ[43,44] basis sets. Geometries were optimized, and normal modes were calculated for all of the structures. Cartesian coordinates of three stable dimer structures can be found in Table S1.

Calculations for the unit cell and also for the isolated single molecule were performed using CRYSTAL09[45] at the DFT (B3LYP) level of theory using the 6-31G(d,p) basis set. It is to be noted that CRYSTAL09[45] has the option of calculating the energy parameters both for a single molecule and also for the entire unit cell involving periodicity. There are several advantages in this approach, which allow for a direct comparison with the observed crystallographic results. The input coordinates were taken from the single crystal data, and geometry optimization was performed. The resulting coordinates of the optimized conformers are given in Table S2. The infrared intensities of the crystalline HA were computed via the Berry phase approach as implemented in CRYSTAL09.[46,47]

Polarized continuum model (PCM)[13] calculations, in the C-PCM (conductor-like PCM)[14] variety, were carried out (as implemented in Gaussian 03) to characterize the influence of a polar environment on the relative stability of HA conformers. In the C-PCM approach, the solute is placed in a cavity formed by the envelope of spheres centered on the atoms or the atomic groups. Inside the cavity, the dielectric constant is the same as in a vacuum; outside, it takes the value of the desired solvent (ε = 78.39 for water). The geometries of HA conformers in water solution were fully optimized within the C-PCM approach at the MP2/6-311++G(d,p) level. The corresponding vibrational frequencies were calculated numerically.

RESULTS AND DISCUSSION

As indicated before, the initial low-temperature matrix isolation FTIR experiments led to the observation of only the most stable intramolecularly hydrogen bonded Cc conformer.[12]

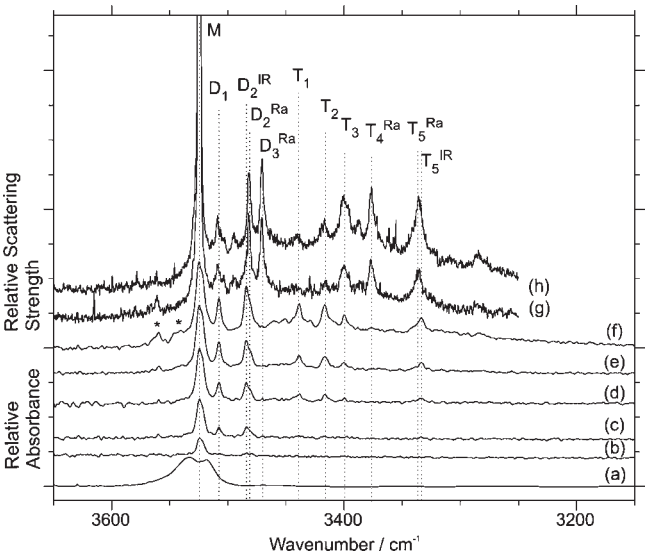

Figure 3. Experimental IR and Raman spectra of HA in the 3650−3150 cm^{-1} region. (a) IR gas-phase spectrum of 0.15% HA in He, measured at 170 mbar. (b−f) IR jet spectra at different HA concentrations in He and a stagnation pressure of 0.7 bar: (b) 0.02%, (c) 0.05%, (d) 0.06%, (e) 0.1%, and (f) 0.15%. (g,h) Raman jet spectra at different clustering conditions in He: (g) 0.15%, 2 mm nozzle distance; (h) 0.2%, 2 mm nozzle distance. Possible HA/H_2O clusters are marked with "*".

The performed theoretical analysis, also, prompted that it might be possible to populate the higher energy Tt form. This was achieved in a later experimental study,[48] where the higher energy Tt form was populated with the help of narrowband selective IR irradiation. This higher energy form could also be converted back to the low energy Cc form using the same procedure. Also, we know from the previous theoretical[10,49a] and experimental studies on HA[7,11,50] that the molecule may change its conformational preference upon aggregation. In the present section, we shall discuss the effect of aggregation on the conformational isomerism in HA observed using different experimental as well as theoretical techniques.

Small Aggregates in a Supersonic Jet. We start with the discussion of small aggregates formed during supersonic jet expansions. The jet spectra were recorded (using helium as carrier gas) in the 3800−3200 and 2000−1000 cm^{-1} spectral regions. OH stretching jet FTIR spectra are shown in Figure 3 for different concentrations of HA in helium at 0.7 bar stagnation pressure. Also shown in the figure is the gas-phase spectrum (trace a) of HA for comparison. It was not possible to obtain spectra without H_2O impurity, but a controlled measurement of HA/H_2O mixtures enabled us to identify the dominating spectral features of mixed clusters (marked with "*"). As can be seen from Figure 3, the jet spectra involve monomers as well as aggregates. The single prominent peak (M) at 3525 cm^{-1} in the highest dilution spectrum shown in trace (b) is largely due to HA monomer. An increase in the concentration of HA results in the appearance of two additional bands (D_1, D_2^{IR}, including a shoulder D_2^{Ra}) followed by a set of peaks (T_1, T_2, T_3, T_5^{IR}) at even higher concentration (traces (c)−(f)). Initially, the T bands are an order of magnitude weaker than the D peaks. At the highest concentration, the difference is only about a factor of 2. Taking into account this different intensity change with concentration, it is likely that the D peaks are due to dimers and the T peaks are due to larger clusters.

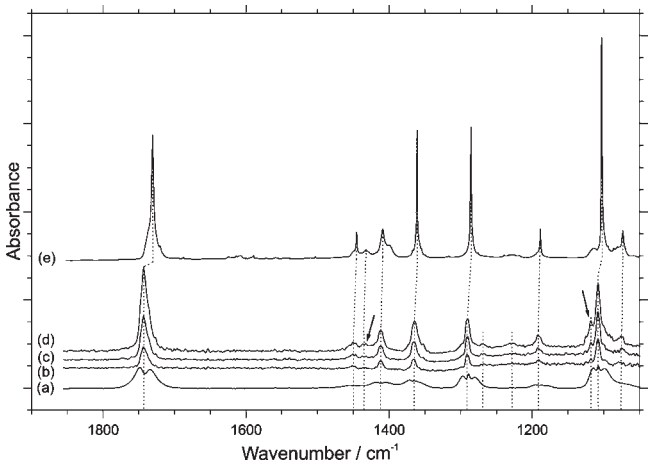

Figure 4. Experimental IR spectra of HA in the 1900−1050 cm^{-1} region. (a) Gas-phase spectrum of 0.15% hydroxyacetone in helium, measured at 170 mbar; (b−d) jet spectra for different HA concentrations in helium: (b) 0.05%; (c) 0.01%; and (d) 0.15%, measured with 0.7 bar stagnation pressure and (e) spectrum of HA in an argon matrix. Possible cluster features are marked with arrows.

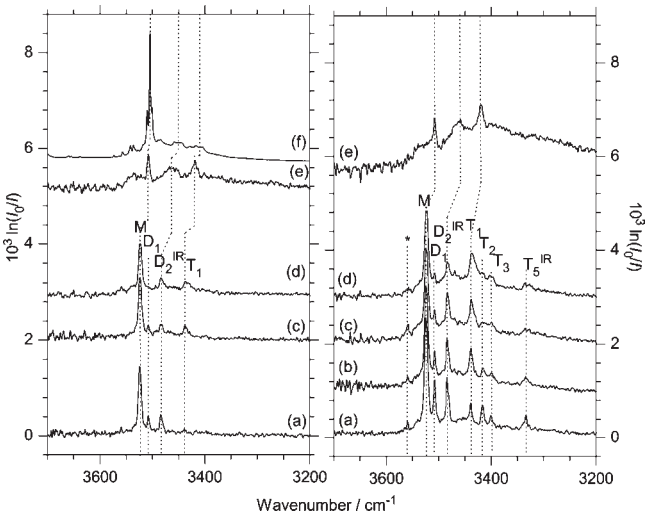

Figure 5. Experimental IR spectra of HA in the 3700−3200 cm^{-1} region as a function of the argon admixture, measured with a stagnation pressure of 0.7 bar and a concentration of 0.05% (on the left) or 0.1% (on the right) HA in He. (a) 100% He, (b) 1% Ar in He, (c) 2.5% Ar in He, (d) 5% Ar in He, (e) 100% Ar, and (f) HA in Ar matrix, scaled by 0.005. Possible HA/H_2O clusters are marked with "*".

The peak due to the OH stretching vibration of matrix isolated HA monomer appeared at 3505 cm^{-1},[12] 20 cm^{-1} red-shifted as compared to the jet spectrum. This relatively large frequency shift of the OH stretching vibration is matrix-induced and shows sensitivity of the OH hydrogen bond to the environment.

Figure 4 shows the supersonic jet spectra of HA in the fingerprint spectral region (b−d) along with the gas-phase spectrum (a) and a matrix spectrum (e). The jet spectra in this range were recorded under conditions similar to those of the OH stretching region spectra. A narrowing of the rotational structure from that in the gas-phase spectrum is observed upon supersonic expansion. The lack of intensity enhancement upon intermolecular hydrogen bonding makes it difficult to identify clusters in the fingerprint spectral range, although the bands marked with arrows may have a cluster origin, as they are not evident in the room-temperature gas-phase spectrum. The comparison of trace (a) with the matrix isolation spectrum (e) shows that matrix shifts are nonsystematic, but always to a lower wavenumber. It also reveals minor cluster contributions in the matrix. Clearly, the OH stretching region is more suitable for the identification of the formed clusters due to its hydrogen-bond sensitivity.

Argon admixture to the helium expansions can be helpful in the identification of stable clusters,[4−6] promoting relaxation to the thermodynamically favored conformations. At higher concentrations of argon, the studied molecules can be coated with Ar shells, resulting in a nanomatrix environment around the clusters. While the relaxation effect should lead to relative intensity changes, the coating typically results in frequency shifts and a broadening of the bands. Both effects are observed in the present case (Figure 5). Two different concentrations of HA in the carrier gas (0.05% and 0.1%) were employed (the spectra are shown in the left and right panels of Figure 5, respectively). The Ar/He ratio in the carrier gas was varied from 0% (trace (a), bottom) to 100% (trace (e), top). While peak D_2^{IR} and perhaps also D_2^{Ra} persist with increasing Ar content, peak D_1 disappears. This must be attributed to the fact that peak D_1 is due to a less stable dimeric species, which upon collision with Ar atoms is relaxed to a more stable structure (peak D_2^{IR}). Similarly, in the larger cluster region, only peak T_1 persists while the other peaks diminish, which suggests that more than one larger cluster is formed in helium expansions. With increasing Ar concentration ((d) to (e)), a frequency shift of the different absorptions is observed, due to the formation of an argon nanomatrix around the monomer and aggregates. Ultimately, jet expansions of HA in neat argon (trace (e)) are compared to aggregated HA in cryogenic argon matrix (trace (f)). It is clear from trace (f) that besides the monomer peak at 3505 cm^{-1}, some more peaks can also be seen, at 3484 and 3458 cm^{-1}. These peaks can very well be correlated with the absorptions due to clusters in the supersonic expansion spectra.

A valuable assignment aid is provided by Raman jet spectra, shown in traces (g) and (h) of Figure 3. This is due to the different intensity pattern in Raman scattering, which allows for conclusions about the hydrogen-bond topology. The monomer band M is observed at the same position, as expected. The D_1 band is weaker in the Raman spectrum and the D_2^{IR} band vanishes completely, whereas a new peak D_3^{Ra} emerges at the low frequency end of the dimer region. The D_2^{Ra} band, which is only a shoulder in the IR spectrum, becomes rather strong in the Raman experiment. This constellation of peaks suggests, like the argon relaxation experiments, the presence of two or even more different dimer structures. In particular, the D_2^{IR}/D_3^{Ra} pair appears to belong to a symmetric cluster with strong symmetric OH stretching in the Raman (D_3^{Ra}) and strong antisymmetric OH stretching intensity in the IR spectra (D_2^{IR}).[15] In contrast, the D_2^{Ra} and D_1 peaks are probably due to nonsymmetric clusters. At this point, a calibration origin of the difference between D_2^{IR} and D_2^{Ra} can be safely ruled out, as there are no corresponding differences in other peaks and the IR shoulder fits the Raman peak.

In the larger cluster region, there is a similar pattern of Raman/IR correspondence (T_2, T_3), strong intensity difference (T_1, T_4^{Ra}), and slightly shifted bands (T_5^{Ra}, T_5^{IR}). As the next possible cluster size refers to the aggregation of three monomer units, it seems plausible to suggest an assignment to trimer structures. The combined IR and Raman data indicate in this case the presence of one symmetric (T_1, T_4^{Ra}) and at least one asymmetric (T_2, T_3, T_5) trimer.

Table 1. Relative Energies ΔE and Dissociation Energies D of the Most Stable Dimer and Trimer Conformations of HA into Cc Monomer Units in kJ mol^{-1}, without (ΔE_e, D_e) and with Zero-Point Vibrational Energy Corrections (ΔE_0, D_0)[a]

			MP2/6-311+G(d)				B3LYP/6-311++G(d,p)				MP2/aug-cc-pVTZ	
	sym	intermol H-bonds	ΔE_e	ΔE_0	D_e[b]	D_0[c]	ΔE_e	ΔE_0	D_e[d]	D_0[e]	ΔE_e	D_e[f]
D_{A1}	C_1	1	0.00	0.00	49.64	41.28	2.00	1.85	22.43	16.71	0.0	39.0
D_{C2}	C_2	2	6.56	4.27	43.08	37.01	0.00	0.00	24.44	18.56	2.2	36.8
D_{A2}	C_1	1	7.92	5.19	41.71	36.09	5.36	3.79	18.88	14.77	4.3	34.7
D_{S3}	C_1	0	7.90	5.73	41.72	36.11					4.5	34.5
D_{S4}	C_i	0	8.01	5.84	41.63	35.44	8.56	7.02	15.88	11.54	1.8	37.2
D_{S5}	C_2	0	9.25	6.43	40.39	34.86	11.50	9.13	13.16	9.43	4.3	34.7
D_{S6}	C_1	0	10.17	7.34	39.47	33.94	10.37	7.64	14.07	10.92	2.2	36.8
D_{S7}	C_i	0	13.69	8.85	35.94	32.44	12.45	8.91	11.99	9.65	4.0	35.0
Tr_{C3}	C_3	3	0.00	0.00	119.12	100.94	0.00	0.00	54.56	42.01		
Tr_{as1}	C_1	2	4.37	1.71	114.75	99.23	4.67	2.70	49.89	39.30		
Tr_{as2}	C_1	3	6.25	2.35	112.87	98.59	7.27	4.85	47.29	37.15		
$Tr_{C3/2}$	C_3	3	7.31	4.31	111.81	96.64	5.89	2.91	48.67	39.09		

[a] The structures are ordered by increasing MP2/6-311+G(d) energy ΔE_0. Monomer references: [b] −267.678616 hartree; [c] −267.588487 hartree; [d] −268.4585439 hartree; [e] −268.369828 hartree; [f] −267.9149421 hartree. Dissociation energies are calculated as [2 × E(monomer) − E(dimer)] for the dimers and [3 × E(monomer) − E(trimer)] for the trimers.

The small wavenumber difference between T_5^{IR} and T_5^{Ra} might be caused by different trimer structures or underlying tetramers. Furthermore, the Raman spectra confirm the larger cluster origin, as the T bands grow relative to the D bands upon increasing the HA concentration.

Argon relaxation experiments using the Raman setup have also been attempted but remained inconclusive: the intensity ratio between the different dimer (and also between the trimer) peaks remained stable. This can be explained by a more narrow range of accessible nozzle distances (2 mm) as compared to the IR (>10 mm).

To facilitate the interpretation of the experimental results, theoretical calculations of HA and its dimers and trimers were carried out. Table 1 summarizes relative energies and dissociation energies into the most stable monomer fragments.

Note that the monomer is not perfectly planar at several levels of calculation, leading to two interconvertible enantiomeric structures. This can give rise to subtle isomerism for the dimers, which was not investigated systematically. Other limitations of the employed theoretical methods are expected to dominate over this issue.

Three different types of hydrogen-bond topology are found to occur among the most stable dimer (D) structures (see Figure 6). The two intramolecular hydrogen bonds can break up in favor of two reciprocal intermolecular O−H···O bonds in a cyclic structure (label C). Only one intramolecular hydrogen bond may be broken to anchor the corresponding monomer at the other intramolecularly hydrogen bonded monomer via an intermolecular hydrogen bond (label A). Finally, both intramolecular hydrogen bonds may be conserved in sandwich structures (label S) with electrostatic and dispersive binding but no hydrogen bonds between the monomers (Figure 6), like in the related lactones.[51]

As Table 1 shows, there is a very close competition between these three hydrogen-bond motifs. Because of large differences in zero-point energy and the slow convergence of electronic energies with basis set at the MP2 level, an uncertainty of the order of at least 3 kJ mol^{-1} in relative energy persists. Part of this uncertainty is caused by very different interaction components in the

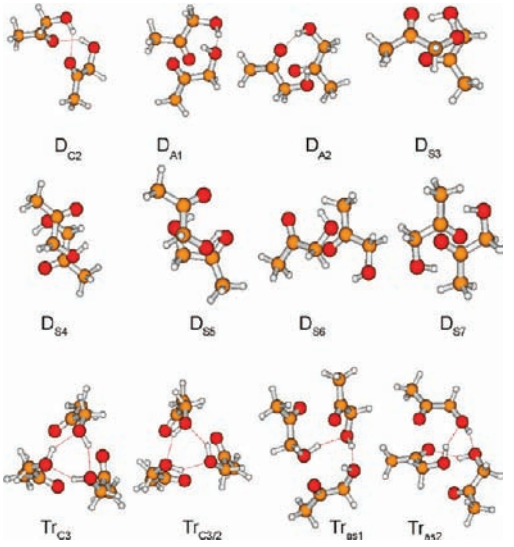

Figure 6. Most stable isolated dimer (D, upper part) and trimer (Tr, lower part) conformations of HA at MP2/6-311+G(d) level. Intermolecular H···O contacts below 2.10 Å are marked with dashed lines. See text for a discussion.

three hydrogen-bond topologies. Isolated hydrogen bonds in C structures are sensitive to the folding of the ring, anchoring hydrogen bonds in A structures are sensitive to cooperative enhancement or anticooperative competition by the intramolecular hydrogen bonds, and S structures are typically underestimated by DFT methods.

Within the 3 kJ mol^{-1} uncertainty window, each of the topologies could actually represent the global minimum structure despite the relatively high level of calculations up to MP2/aug-cc-pVTZ structure optimization. At the B3LYP level, it is a C structure, at the MP2 level, it tends to be an A structure, but zero-point energy favors S structures so much that they become competitive. This should be kept in mind in the following discussion, and indeed experiment is able to provide some constraints on the theoretical predictions if the spectra can be predicted reliably.

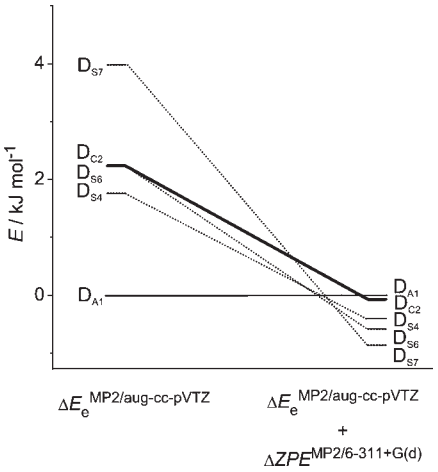

Figure 7. Relative energies of the most stable dimer structures at MP2/aug-cc-pVTZ level. Comparison of energies without zero-point energy correction (left) and energies with MP2/6-311+G(d) zero-point energies (right). Dimers without intermolecular hydrogen bonds are symbolized by dotted lines, dimers with one intermolecular hydrogen bond are shown with continuous thin lines, and D_{C2}, the only structure with two intermolecular hydrogen bonds, is shown with a continuous thick line.

Before starting such a spectroscopic comparison, the three classes of hydrogen-bond topologies shall be analyzed briefly in terms of possible variants.

In the C class, the compactness of the structures is important.[16] This leads to a preference for the folded D_{C2} structure over an inversion-symmetric D_{Ci} variant and also over structures in which the OH group of one monomer is inserted into the intramolecular hydrogen bond of the other, a motif that plays a certain role in related complexes.[52]

In the A class, the anchoring OH may dock at a lone pair of the OH group (D_{A1}) or at a lone pair of the carbonyl group (D_{A2}). The latter variant is anticooperative, as two OH groups compete for electron density of the carbonyl oxygen. This explains why D_{A1} is invariably more stable and a strong candidate for the global minimum.

The S structures are quite diverse and may be divided into two variants, homodromic and heterodromic variants, depending on whether the intramolecular hydrogen-bonded rings have the same or opposite turning sense (clockwise vs anticlockwise pattern of O−H···O═CC). Both variants contribute to the most stable structures. In summary, a folded C structure (D_{C2}), a cooperative A structure (D_{A1}), and sandwich structures (D_{S4}, D_{S6}, and D_{S7}) are among the most promising dimer arrangements to be observed in a supersonic jet expansion. As shown in Figure 7, harmonic zero-point energy corrections using a smaller basis set scramble the energy sequence rather completely even at the MP2/aug-cc-pVTZ level, not to mention possible anharmonic corrections.

Trimer structures (Figure 6) have not been explored exhaustively, but the C_3-symmetric O−H···O−H···O−H arrangement appears to be most stable, like in the related lactate case.[53] However, asymmetric structures with an O−H···O−H···O═C pattern (Tr_{as1}) or a cyclic O−H···O−H···O−H···O═C arrangement (Tr_{as2}) are too close in energy to be neglected, given the very approximate character of the calculations. Note that $Tr_{C3/2}$, the fourth trimer structure in Table 1 (see also Figure 6), is related to the sandwich dimers in not requiring any opening of the intramolecular hydrogen bonds. Like the sandwich dimers, it has a remarkably low energy.

Spectral predictions (Figure 8) are important, but clearly handicapped by the lack of the spectrally reliable B3LYP approach in reproducing the correct structures and by the need of large basis sets for reliable MP2 spectral predictions. Therefore, most of the following discussion concentrates on qualitative and symmetry arguments rather than exact matches between theory and experiment.

In the case of dimers, the qualitative expectation is clear-cut. D_{C2} should have a pair of OH stretching transitions, where the higher frequency band dominates in the IR and the lower frequency band prevails in the Raman spectrum. The splitting is a sensitive measure for the coupling between the two oscillators. At the B3LYP level, it amounts to 23 cm^{-1} and at the MP2/6-311+G(d) level to 18 cm^{-1}. This compares moderately well to the experimental splitting between D_3^{Ra} and D_2^{Ra} bands of 13 cm^{-1} and is more reasonable than the combination of D_1 and D_3, which would translate into an experimental splitting of 37 cm^{-1} and a too high Raman intensity in the case of the higher frequency peak.

D_{A1} is predicted to have a similar intensity pattern in IR and Raman spectroscopy, with a weak absorption closer to the monomer peak and a strong one further red-shifted. This fits the observation of peak D_2^{Ra}, which is strongly visible in both IR and Raman spectra. Although mixed H_2O/HA dimers also contribute in this region, their contribution to D_2^{Ra} and D_2^{IR} can be safely neglected according to the impurity studies mentioned before.

This leaves us with D_1, which shows only a small red shift of −17 cm^{-1} from the monomer and is visible in both IR and Raman spectra but disappears upon Ar relaxation. Overlapping OH stretching bands of kinetically favored sandwich structures are conceivable, as is the anticooperative D_{A2} dimer. A final assignment is not possible at this point.

Higher level harmonic calculations and possibly even anharmonic corrections are needed to match the experimental spectra. The OH stretching anharmonicity changes as a function of hydrogen-bond formation.[54] From a comparison of relative computed and observed intensities of monomers and dimers (see Figure 8), the expansion contains at least 15% dimers. Possible overlap with the monomer band renders this estimate a lower bound. In summary, while the metastable dimer origin of the IR- and Raman-active D_1 band remains uncertain, the assignment of D_2^{IR}, D_2^{Ra}, and D_3^{Ra} to the hydrogen-bonded D_{C2} and D_{A1} structures is quite clear. They appear to be similar in energy or at least difficult to relax to other structures. Whether or not they compete with or even lose against sandwich structures remains to be investigated.

Turning now to the trimers, the spectral interpretation actually becomes more straightforward, like in the methyl lactate case.[5] The exclusively Raman active band T_4^{Ra} is a strong candidate for the C_3 symmetric trimer T_{C3}, which was found to have the lowest energy. As T_1 is the main IR band surviving Ar relaxation, it could be its IR complement. The Davydov splitting[55] is 63 cm^{-1}, which should be compared to the B3LYP prediction of 59 cm^{-1} and the MP2 prediction of 53 cm^{-1}. T_2, T_3, and T_5 would then be due to less symmetric structures like T_{as1} and T_{as2}, but larger cluster contributions, in particular to T_5, cannot be ruled out. In summary, the predicted energetic dominance of T_{C3} with its HOCC torsional angle of 86° is consistent with the experimentally observed feature, but a detailed assignment of the coexisting

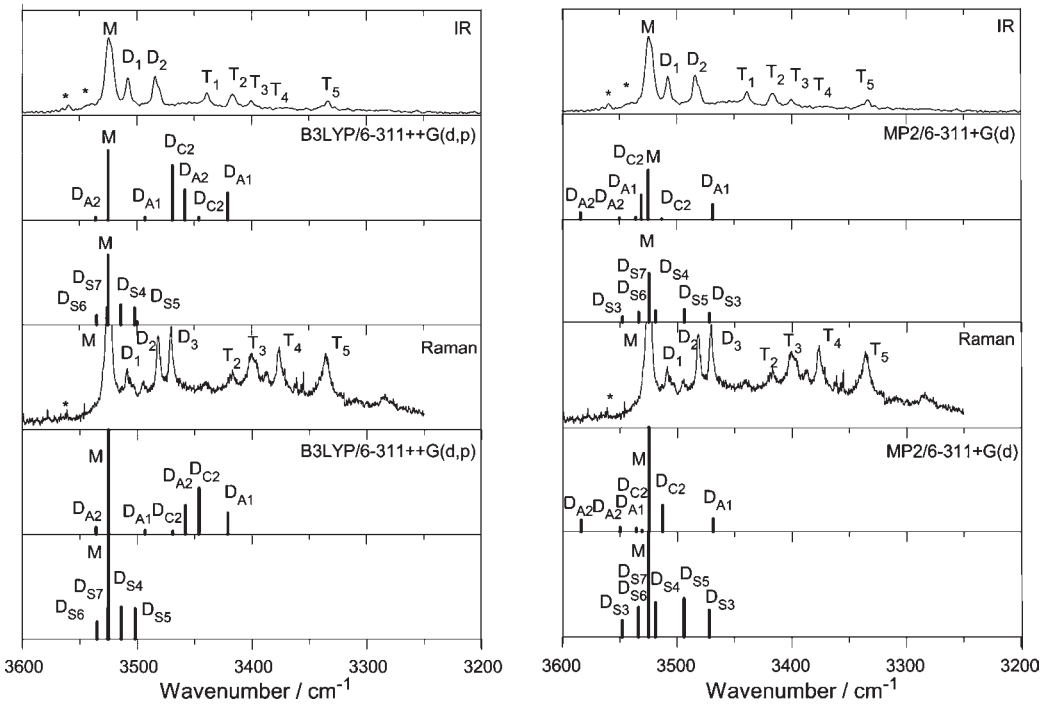

Figure 8. Simulated spectra of HA aggregates in the 3600−3200 cm^{-1} region, calculated at different levels of theory. The simulated spectra are shifted, matching the OH stretching transitions of the monomer to experiment and including the most stable HA dimer structures. The intensities of D_{C2}, D_{A1}, and D_{A2} are scaled by 0.05, and all other dimer intensities by 0.15. The different scaling factors are chosen because, during the sandwich dimer formation, no internal hydrogen bond has to be broken, so they should be kinetically favored.

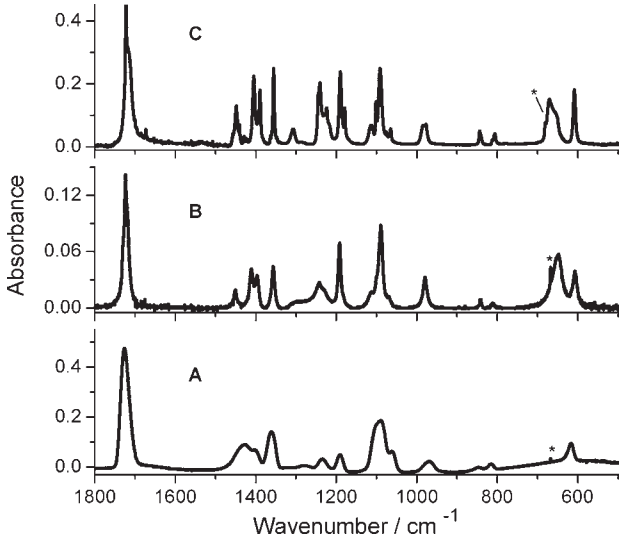

Figure 9. Experimental spectra of HA obtained after deposition at 12 K (frame A) followed by annealing up to 175 K (frame B) and a subsequent cooling to 13 K (frame C). Changes in the spectra are indicative of formation of more ordered crystal (frames B and C) from a disordered form (frame A). The band marked with an asterisk is due to atmospheric CO_2.

conformations remains open. Structurally, the OH group in T_{C3} is clearly rotated further out of the OCCO plane than in the dimers.

It is interesting to note that for several of the energetically competitive dimer structures and for all of the competitive trimer structures, upon aggregation the intramolecular hydrogen bond O−H···O═C opens up in favor of one or two intermolecular hydrogen bonds, so at least in one of the molecules, the hydrogen atom of the hydroxyl group is out of the heavy-atom plane. This result agrees with the work carried out on similar compounds,[4−6] which suggests that molecules like HA have a tendency to undergo conformational change upon complex formation. In the present case, intermolecular hydrogen bonds of the type O−H···O−H and C═O···H−O are seen to be established between the structural motifs causing different types of clusters (Figure 6). This result is also in agreement with the statements made by Jetzki et al.[7] and Mohaček-Grošev[11] that aggregation in HA may result in the breaking up of the intramolecular hydrogen bond.

Bulk Solids (FTIR). In continuation of our effort to understand conformational changes upon aggregation in HA, a low-temperature FTIR study of solid HA was conducted. The experimental spectra are shown in Figure 9. Initially, fast deposition of the compound vapor onto the cold (12 K) CsI window of the cryostat is done (Figure 9, frame A). The sample is then subjected to annealing up to a temperature as high as 175 K (Figure 9, frame B) followed by cooling to 13 K, at which a highly ordered crystal is obtained (Figure 9, frame C). During this heating → cooling cycle, bands in the spectrum undergo gradual changes, as shown in Figure 10. In most of the regions, cooling from 175 to 13 K leads mainly to transformation of broad bands due to a less ordered assembly into sharper peaks ascribable to a highly ordered crystal. In the region 1050−940 cm^{-1}, a single band is transformed into a doublet near the temperature of 75 K. A similar behavior is observed in the CH bending region 1470−1430 cm^{-1}. These changes are found to be irreversible, in the sense that a subsequent increase of temperature does not revert the spectral profile to that observed immediately after deposition

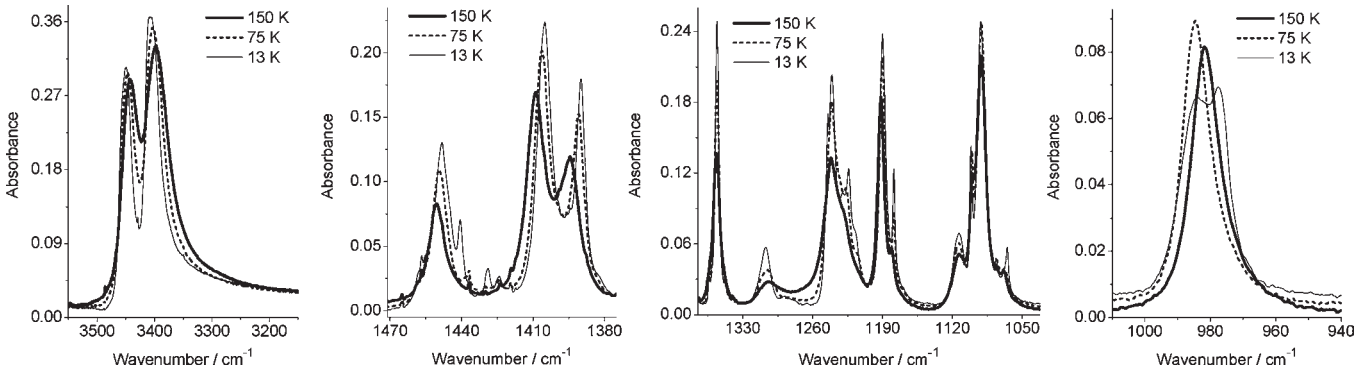

Figure 10. Selected ranges of the experimental IR spectra observed in OH stretching and fingerprint regions during crystallization of HA. After deposition at 12 K (spectra not shown in this figure, see Figure 9A), HA is subjected to annealing up to the temperature of 175 K followed by cooling to 13 K. The spectral changes shown above are those observed during cooling.

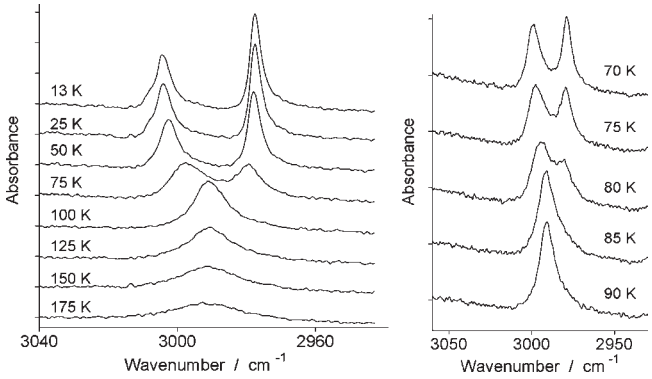

Figure 11. Spectral changes observed in the CH stretching region of neat HA while cooling from 175 K (deposition temperature) to 13 K (left frame). One can see the drastic change in the spectrum around 3000 cm^{-1} between temperatures 100 and 75 K. This change is found to be reversible. Right frame shows a blown up representation of this spectacular change occurring between 100 and 70 K.

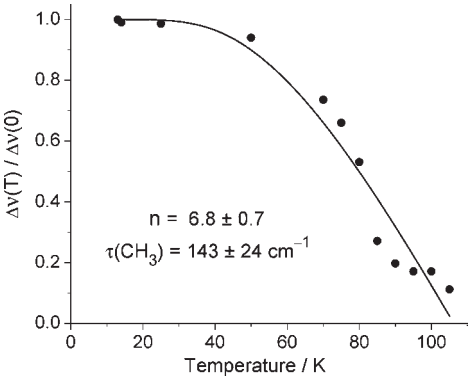

Figure 12. $\nu(CH_3)_{as}$ reduced band splitting as a function of temperature for HA in the neat crystalline state (●) and calculated fit to the data according to the Redfield theory.[56,58−61] In the fit equation (eq 1), n and the $\tau(CH_3)$ wavenumber (ν_τ) were considered as parameters in the fit, while the rotational constant B was taken to be that for an "uncoupled" methyl rotor, being equal to 5.3 cm^{-1}.[56,62] The squared correlation coefficient of the fit is $R^2 = 0.954$.

of the sample. A different behavior is seen in the CH stretching region around 3000 cm^{-1} (Figure 11). In a separate experiment, sample was deposited at 175 K and then was cooled to 13 K. In the spectrum of the deposited sample, a broad band appears around 3000 cm^{-1}, which begins to gain peak intensity with cooling. This band becomes asymmetric upon temperature decrease and starts to noticeably split into two bands at ca. 90 K. The doublet hence formed then persists down to the lowest temperature attainable in our setup (∼10 K), the relative intensities of the component bands and their relative position changing in a continuous way (Figure 11). The more interesting feature of these spectral changes is their reversibility, that is, upon subsequent cycles of rewarming/recooling, the spectral profile in this region changes as shown in Figure 11. The same behavior was observed during the warming→recooling cycle in the experiment where the sample was deposited at 12 K as well as during cooling of the sample deposited at 175 K. Hence, both experiments resulted in the same crystal structure.

Analogous behavior of CH stretching bands of methyl groups as a function of temperature has been reported in studies carried out on a number of alkane systems.[56,57] In those studies, two bands were observed for the CH asymmetric stretching of the methyl group ($\nu(CH_3)_{as}$) at low temperatures, which coalesce in a reversible way into a single band upon raising the temperature. MacPhail et al.[56,57] attributed these changes predominantly to the intramolecular coupling between the CH stretching modes and the methyl torsion. In particular, the observed collapse of the bands due to the CH asymmetric stretching methyl modes can be expected to take place upon the triggering of the methyl group free internal rotation at a given temperature. The two methyl asymmetric vibrations are nondegenerate in a C_s or C_1 local symmetry environment, but become degenerate when the local symmetry turns to C_{3v}.

Increase of temperature changes the local symmetry of the methyl group in HA, due to the onset of its free internal rotation, and the two bands appearing at ca. 3005 and 2978 cm^{-1} in the HA crystal (which were assigned to the two asymmetric stretching vibrations of the methyl group[12]) collapse, giving rise to a single broad band with maximum around 2990 cm^{-1} (Figure 11).

Figure 12 shows the plot of $\nu(CH_3)_{as}$ reduced band splitting $\Delta\nu(T)/\Delta\nu(0)$ as a function of temperature (T) for HA in the neat crystalline state. In this plot, the band splitting at 0 K was approximated by the band splitting at the lowest work temperature (13 K). The figure shows also the calculated data fit according to the Redfield theory.[56,58−61] In the fit equation (eq 1), the coupling

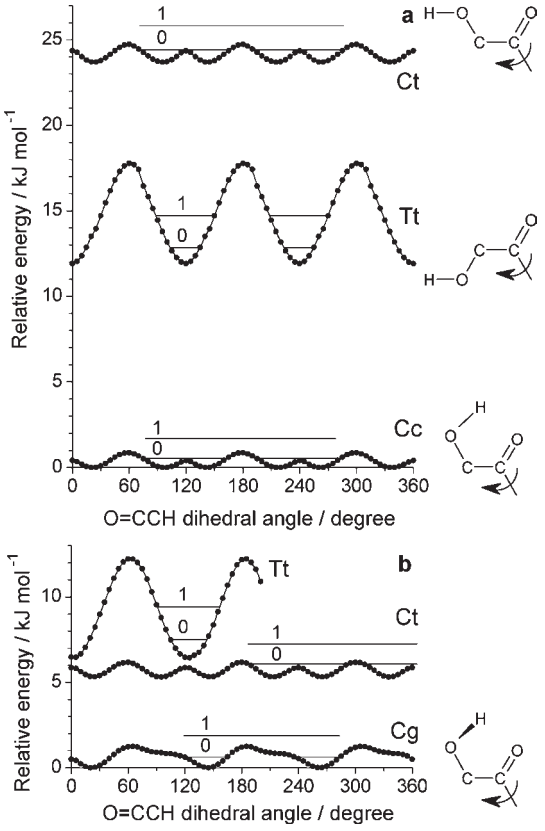

Figure 13. Relaxed potential energy scans for internal rotation of the methyl group (designated by arrows) in different conformers of HA calculated at the MP2/6-311++G(d,p) level of theory for (a) monomer in the gas phase, and (b) monomer in a polar environment (polarized continuum model, solvent = water). The horizontal lines marked by 0 and 1 designate the vibrational ground states and the first excited vibrational levels, respectively, calculated for the internal methyl torsion in the harmonic approximation. A part of the potential energy profile of Tt form is suppressed in frame (b). Note that conformer Cc corresponding to vacuum (frame a) transforms into Cg in the polar environment (frame b).

parameter n (which relates with the local periodicity of the torsional potential energy profile) and the frequency of the methyl torsion (ν_τ) were considered as the parameters, while the rotational constant B was taken to be that for an "uncoupled" methyl rotor, being equal to 5.3 cm^{-1}.[56,62]

$$\frac{\Delta\nu(T)}{\Delta\nu(0)} = \frac{1 - \dfrac{n^2B}{2\nu_\tau}\coth\dfrac{\alpha}{2}}{1 - \dfrac{n^2B}{2\nu_\tau}}, \text{where } \alpha = hc\nu_\tau/kT \qquad (1)$$

The fitted values for n and ν_τ were 6.8 ± 0.7 and 143 ± 24 cm^{-1} (R^2 = 0.954). As shown below, these values are close to the expected intramolecular methyl torsion periodicity of six, predicted for Ct in a polar environment, and to the DFTcalculated torsional frequency of a Ct-based crystal (~200 cm^{-1}). They are also consistent with the very low torsional barrier of the methyl group in the Ct conformer.[8,9,63]

Figure 13a shows the potential energy profiles for the internal rotation of the methyl group in case of Cc, Tt, and Ct structures calculated in the gas-phase approximation. For conformer Tt, one full rotation of the methyl group produces three local minima, corresponding to the eclipsed position of the C═O group with alternating hydrogen atoms of the methyl group.

The calculated methyl torsion barrier for this conformer is 491 cm^{-1}. For Cc and Ct structures, there are six local minima per one 360° rotation. This is related to the fact that neither the eclipsed nor the staggered orientation of the C═O and CH (methyl) groups is energetically favorable. As a result, the minimum energy conformation is realized for an intermediate orientation between eclipsed and staggered geometry, near the perpendicular orientation of the O═CCH angle (~90°). Considering that the perpendicular orientation can be realized for both clockwise and anticlockwise rotation, and for any of the three CH bonds of the methyl group, the 6-fold minimum energy profiles arise for Cc and Ct. The high density of the local minima implies that they are separated by low-energy barriers. Indeed, the MP2/6-311++G(d,p) calculated barriers for Cc and Ct structures amount to only 71.9 and 87.8 cm^{-1}, respectively. Only the vibrational ground states of the methyl torsion barely fit within the barriers (Figure 13a). Already the first excited torsional level (transition energies of 90.6 cm^{-1} (Cc) and 118.4 cm^{-1} (Ct) calculated for the gas phase in the harmonic approximation) is situated above the barrier. The low energy of the excited torsional levels affords their easy population already at low temperatures (e.g., 15% for Cc at 75 K) and indicates the possibility of free rotation of the methyl group in both Cc and Ct. Indeed, it has been shown[49] that the very low value of the barrier for internal rotation of the methyl group and a very low frequency for methyl torsion allow for large amplitude vibrations in the cryogenic experiments.

The influence of the polarity of the media on the methyl torsion potential energy profiles was also evaluated. Figure 13b shows the profiles calculated for the three most stable HA conformers in the approximation of the polarized continuum model (PCM, solvent = water, ε = 78.39). The profile for the Tt conformer remains almost the same as for the gas-phase calculations, showing only a slight stabilization relative to the most stable conformer. This profile exhibits a 3-fold minimum similar to that shown in Figure 13a, which is partially suppressed to show better other graphical elements.

The calculated profiles for the other two forms, however, exhibit profound changes. The most stable conformer transforms from Cc to Cg. In a polar environment, the geometry around the CCOH dihedral angle assumes a gauche orientation and indicates a partial break-up of the intramolecular hydrogen bond. This also introduces asymmetry in the internal rotation of the methyl group. Unlike for Cc in the gas phase, the clockwise and anticlockwise "perpendicular" orientations of the O═CCH dihedral angle become unequal for Cg. A more stable geometry corresponds to the combination of the CCOH and O═CCH dihedral angles approximately equal to +60° and −90° (or 270° in Figure 13b), respectively (the value of CCOH dihedral angle stays in an interval of 1° centered around 54.2°). The 6-fold minimum profile of Cc in the gas phase is substituted by a 3-fold minimum profile for Cg in water environment.

The most spectacular changes are found for the Ct structure. Upon transition from the gas phase to the polar environment (water), Ct is stabilized by ca. 18 kJ mol^{-1} (compare Figure 13a and b). Ct becomes the second most stable conformation, only 5 kJ mol^{-1} above the most stable structure (Cg). The methyl torsional barriers remain low for Ct and Cg upon transition to the polar environment. Their first excited torsional levels (horizontal lines designated by "1") are related to low transition energies

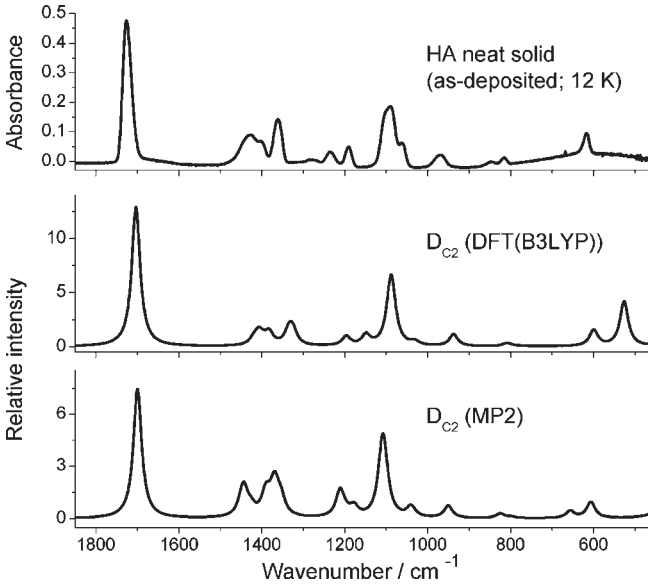

Figure 14. Comparison of the experimental spectrum of neat solid HA obtained by deposition at 12 K of vapor of the compound (top) with the spectra of dimer D_{C2} simulated with Lorentzian functions (fwhm = 25 cm^{-1}). The calculated DFT(B3LYP) and MP2 wavenumbers are scaled by a factor of 0.96. The basis set used was 6-311++G(d,p).

(about 1 kJ mol^{-1}) and lie above the top of the barriers, indicating easy access to a free rotation of the methyl group. The most interesting result yielded by the PCM calculations is that only the Ct form conserves the 6-fold periodicity of the methyl torsional profile. This result, in combination with the Redfield theory simulation of the $\nu(CH_3)_{as}$ dependence on temperature, indicates Ct as the most probable structure that is assumed by HA molecules in the crystal.

Furthermore, there is an additional piece of information that allows us to safely eliminate Cc (or Cg) from being the constituent of the crystalline phase of HA. As already discussed, the spectrum obtained after the direct deposition at 12 K is much different from the one obtained after annealing and subsequent recooling of the deposited sample (Figure 9). This spectrum of HA obtained by deposition at 12 K is indeed quite comparable with the simulated spectra of dimer D_{C2} (Figure 14) obtained using both MP2 and DFT methods. This fairly good agreement between the observed spectrum of the deposited neat film of the compound and the simulated spectra of D_{C2}, where the HA molecules adopt a Cg structure, clearly indicates the presence of a partially open Cg structure in the unorganized deposited solid of HA at 12 K. This can be explained assuming that Cc conformers, dominating in the gas phase of HA, undergo initially only a small structural change when deposited onto the cold substrate of the cryostat. This small change consists of a partial break-up of the intramolecular hydrogen bond and allowing the hydroxyl hydrogen atom to rotate by ca. 60°, from cis to gauche, which is sufficient to establish dimers. At this stage, such reorganization is energetically favorable and accessible. The complete relaxation into the most stable structure in the condensed phase should require the reorientation of a large number of HA molecules and is energetically not accessible at cryogenic temperatures of the order of 15 K. Such reorganization turns possible only upon annealing of the samples up to 80 K and above. It manifests itself by a considerable change of the IR spectra after the annealing, and this

Table 2. Relevant Bond Lengths, Bond Angles, and Torsion Angles of Hydroxyacetone (Ct Conformer) as Obtained from X-ray Experiment and Theoretical Calculations

atom labels	X-ray	CRYSTAL09
	Bond Length (Å)	
H2−O2	0.760(3)	0.975
O2−C3	1.403(2)	1.406
C3−H1	0.919(16)	1.099
C3−C2	1.495(3)	1.508
C2═O1	1.218(2)	1.226
C2−C1	1.499(3)	1.508
C1−H3	0.890(2)	1.094
C1−H4	0.910(3)	1.091
	Bond Angle (deg)	
C3−O2−H2	110.91(19)	108.08
C2−C1−H3	109.72(14)	109.12
C2−C1−H4	112.0(2)	111.71
H3−C1−H4	108.5(17)	109.22
O2−C3−C2	110.58(15)	110.48
O2—C3−H1	112.64(10)	112.53
C2−C3−H1	106.30(10)	107.47
O1−C2−C3	121.46(16)	121.47
O1−C2−C1	122.52(16)	122.37
C3−C2−C1	116.02(16)	116.16
	Torsion Angle (deg)	
O2−C3−C2−O1	0	0
O2−C3−C2−C1	180	180
H2−O2−C3−C2	180	180

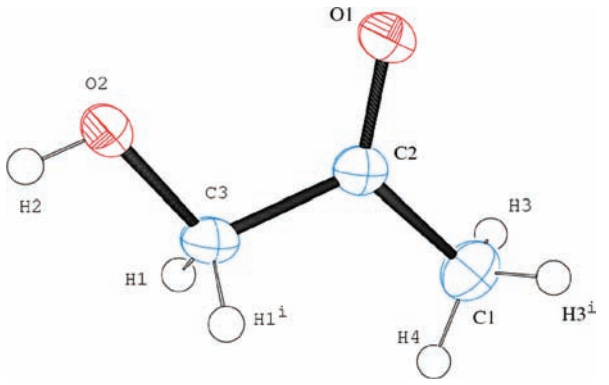

Figure 15. ORTEP diagram with 50% ellipsoid probability along with atom numbering scheme used for crystal calculations. Hydrogen atoms are drawn as arbitrary circles.

considerable change persists after the subsequent cooling. Hence, we can conclude that the Cg-based metastable structures, existing in the freshly deposited neat HA, disappear after this procedure, giving rise to a new structural motif based, with all probability, on Ct structure. Hence, as a whole, the neat solid-state HA results point to Ct as the structure assumed by HA molecules in the crystalline state. The confirmation of this was

Table 3. Hydrogen-Bonding Features Obtained from X-ray Experiments as well as Theoretical Analysis[a]

D−H···A[b]	D···H/Å	D···A/Å	H···A/Å	∠D−H···A/deg	symmetry
O2−H2···O1	0.76(2)	3.018(2)	2.35(2)	148	$x-1/2, -y+1/2, -z+1/2+2$
$O_h-H_h\cdots O_c$	*0.975*	*3.061*	*2.235*	*141.79*	$x-1/2, -y+1/2, -z+1/2+2$
O2−H2···O2	0.76(2)	2.843(2)	2.21(3)	142	$x-1/2, -y+1/2, -z+1/2+2$
$O_h-H_h\cdots Q_h$	*0.975*	*2.848*	*2.022*	*141.22*	$x-1/2, -y+1/2, -z+1/2+2$

[a] The values obtained from theory (CRYSTAL09) are shown in italics [O_h (oxygen of the hydroxyl group), O_c (oxygen of the carbonyl group), H_h (hydrogen of the hydroxyl group)]. [b] D − hydrogen donor atom, A − hydrogen acceptor atom.

Table 4. Crystallographic Details

formula	$C_3H_6O_2$
CCDC no.	733430
formula weight (g mol^{-1})	74.1
temperature (K)	110
wavelength (Å)	0.71073
crystal system	orthorhombic
space group	*Pnma*
a (Å)	5.4648(24)
b (Å)	6.4096(28)
c (Å)	10.9837(48)
volume (Å^3)	384.73(3)
Z	4
density (g/cm^3)	1.28
F(000)	160.0
$\theta_{min,max}$	3.7,26.0
$h_{min,max}$	(−6,6)
$k_{min,max}$	(−7,7)
$l_{min,max}$	(−11,13)
no. of measured reflections	2239
no. of unique reflections	410
no. of parameters	45
R_{all}, R_{obs}	0.045, 0.038
wR_{2all}, wR_{2obs}	0.093, 0.090
$\Delta\rho_{min,max}$ (e Å^{-3})	0.224, 0.224
GOF	1.097

achieved by using the X-ray diffraction technique, as described in the next section.

X-ray Crystallography and Cognate Theoretical Studies. The spectroscopic studies described so far invite a complementary low-temperature in situ cryocrystallization study. HA crystallizes in the centrosymmetric space group *Pnma* in the orthorhombic crystal system with $Z = 4$. Figure 15 shows the thermal ellipsoid plot with atom numbering. Table 2 lists all of the geometrical parameters of HA obtained from both crystal structure determination and CRYSTAL09[45]-based calculation for the configuration determined from the crystal structure (Ct) analysis. The hydrogen-bonding interactions are given in Table 3. The crystallographic details are listed in Table 4. The HA molecule is characterized by the CCOH dihedral being in the "trans" orientation with respect to O2−C3 bond coinciding with the Ct conformer. It is noteworthy that this particular conformer is absent in the gas phase.[12] The molecule sits on a mirror symmetry at $(x, 1/4, z)$ position excluding H1 and H3 atoms, which are in general positions. The molecular packing is mainly through two types of O−H···O hydrogen bonds represented by bifurcated intermolecular hydrogen-bond patterns, which lead to ring $R^2_1(5)$ and infinite chain $C^2_2(4)$ graph set motifs[64] (Figure 16).

Table 5. (a) Total and Relative Energies of Cc and Ct Conformers for Single Molecule and 3D Unit Cell; and (b) Mulliken Population Analysis Based on the CRYSTAL09 Calculations[a]

(a)

conformers	*E* (hartree)	Δ*E* (hartree)	Δ*E* (kJ/mol)
Single Molecule Calculations			
Cc	−268.22256	0.0	0.0
Ct	−268.21109	0.01147	30.11
3D Unit Cell Calculations			
Ct	−1072.96082	0.0	0.0
Cc	−1072.95145	0.00937	24.60

(b)

	Net Atomic Charge		Bond population (distance)			
			$B(H_O\cdots O_C)$ (d)		$B(H_O\cdots O_H)$ (d)	
Ct	O_C	−0.462				
	O_H	−0.589				
	H_O	+0.372	+0.028	(2.235)	+0.024	(2.022)
Cc	O_C	−0.465				
	O_H	−0.585				
	H_O	+0.352	+0.036	(2.215)	+0.019	(2.208)

[a] 1 hartree ≈ 2625.5 kJ/mol; calculations are done by using the DFT-(B3LYP)/6-31G(d,p) method. The energy values are relative to the most stable structure. O_C, O_H, and H_O are carbonyl oxygen, hydroxyl oxygen, and H-atom of the OH group, respectively. $B(H_O\cdots O_C)$ and $B(H_O\cdots O_H)$ represent the bond population of $H_O\cdots O_C$ and $H_O\cdots O_H$ bonds, respectively. All the quantities are in $|e|$ units, while (d) is the respective bond distance (in Å).

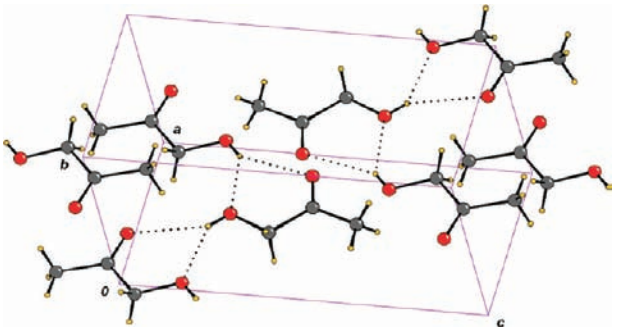

Figure 16. Packing diagram in the unit cell with bifurcated O−H···O intermolecular hydrogen bonds shown by dotted lines.

dx.doi.org/10.1021/ja2030646 |*J. Am. Chem. Soc.* 2011, 133, 20194–20207

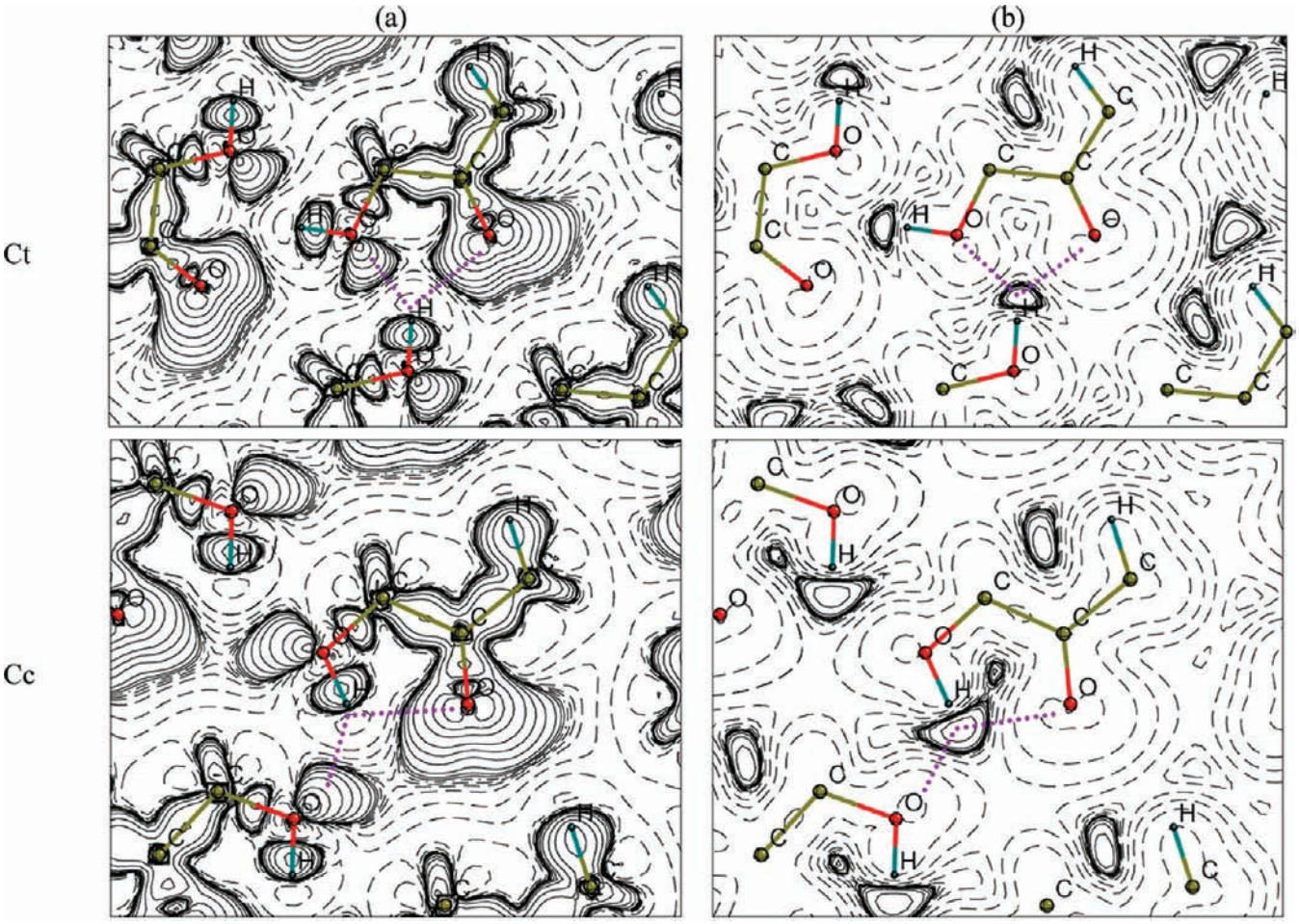

Figure 17. Calculated difference electron density maps (a) and electrostatic potential maps from difference electron density (b) for Ct (top) and Cc (bottom) conformers. The violet dotted lines highlight the hydrogen bonds. The isolines represent negative (dotted lines), positive (continuous lines), and zero (dot-dashed line) values of the electron density (a) and of the electrostatic potential (b) in $|e|/\text{bohr}^3$ units. The maps are drawn in logarithmic scale.

The experimentally observed crystalline system of the Ct conformer was optimized using the CRYSTAL09[45] package. A close examination of Tables 2 and 3 reveals the agreement between the X-ray data and theoretically optimized geometries. It was considered worthwhile to put the Cc geometry in the crystal lattice and evaluate the optimized geometry using CRYSTAL09[45] calculations. In this hypothetical experiment, the coordinates of the hydrogen atom of the OH group were changed from the Ct geometry to mimic the Cc geometry. It was also assumed that the space group might still be retained as *Pnma*. This assumption is questionable; however, it would provide an approximate estimate of the energies involved for the Cc geometry. Single molecule optimization was also carried out for both of the conformers. Table 5 lists the total and relative energies derived for this hypothetical model as compared to the Ct geometry in the crystal structure. It also lists the stabilization energy of Cc conformer in the gas phase as compared to the Ct conformer in the crystalline phase.

The difference electron density maps along with electrostatic potential maps derived from difference electron density are drawn for both of the conformers (Figure 17a and b, respectively). Difference electron density is the difference between the crystal electron density and a "reference" electron density. The "reference" density is taken as a superposition of atomic charge densities. Hence, difference maps show the influence of the crystal packing on the electron density. As a result, the electrostatic potential from the difference electron density clearly brings out subtle intra- and intermolecular interactions present in the crystal better than total electron density (Figure 17b).

The difference electron density maps (Figure 17a) indicate the presence of bifurcated hydrogen bonds in both of the conformers, where the hydrogen atom of the OH group is forming H-bonds with the oxygen atom of the C═O group and the oxygen atom of another OH group simultaneously. In the Ct conformer, the bifurcated hydrogen bonds are intermolecular in nature, while in the Cc conformer O−H···O═C is intramolecular and O−H···O−H is intermolecular in nature. This is analogous to the situation in the trimers Tr_{C3} and $Tr_{C3/2}$ shown in Figure 6. It is obvious that the Cc geometry would form an intramolecular O−H···O hydrogen bond irrespective of the crystallographic space group in which it might crystallize. Yet an interesting feature has come out from electrostatic potential maps as well as Mulliken population analysis. The overlap population values for the hydrogen bonds indicate that both intermolecular hydrogen bonds are equally strong in the Ct conformer, whereas in the Cc conformer the intramolecular hydrogen bond is more favored than the intermolecular one. This nonequality in hydrogen-bond strength minimizes the opportunity for intermolecular hydrogen bond formation in the Cc conformer. The X-ray determined structure

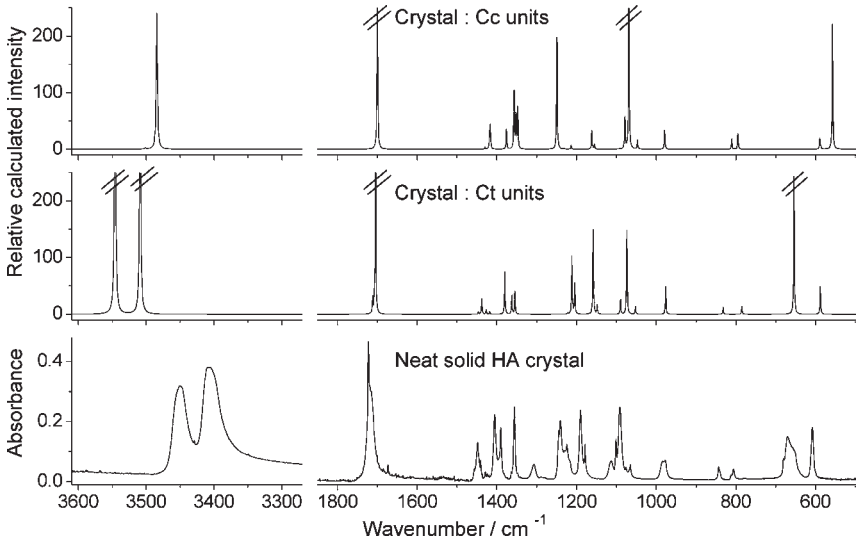

Figure 18. Comparison of experimental spectrum of solid HA at 175 K (bottom) with the simulated spectra of a crystal formed of Ct units (middle) and Cc units (top). Calculated spectra are obtained from the DFT(B3LYP)/6-31G(d,p) method. Some of the simulated bands have been truncated. A close agreement between the spectra in the middle and the bottom frames can be seen. The calculated wavenumbers have been scaled by 0.96.

shows that the Ct geometry is found in the crystal. The theoretical results can reproduce experiment.

Thus, according to both the X-ray results and the theoretical calculations, and in agreement with the information extracted from the low-temperature IR spectroscopic measurements discussed above, the HA crystal is formed of Ct units involved in intermolecular hydrogen bonds (Figure 16). Having this information, a comparison of the observed IR spectrum of crystalline HA is done with the simulated spectra of the crystal formed of Ct units, as obtained from CRYSTAL09.[45] This is shown in Figure 18. A simulated spectrum of the crystal with the Cc units is also shown (top frame). A good agreement between the experimental FTIR (bottom frame) and simulated spectrum of the crystal containing the Ct form (middle frame) can be seen from the figure, especially in the OH stretching region. Occurrence of a doublet in this region in the simulated spectrum of the crystal formed of the Ct units demonstrates a striking similarity between the theoretical (middle frame) and the experimental (bottom frame) spectra. Thus, we can say that the crystals obtained from low-temperature FTIR and in situ cryocrystallization are indeed the same.

CONCLUSION

The present study is focused on the conformational isomerism in HA, from the gas phase to the solid state, as a result of aggregation. Various experimental as well as theoretical methods were employed to study the aggregation patterns and, hence, the conformational changes in the present molecule. Supersonic jet expansions with helium and argon as carrier gases were employed to identify and characterize different forms of clusters formed. Assignment of the bands was facilitated by quantum chemical calculations carried out at DFT (B3LYP) and MP2 levels of theory. HA, which exists as an intramolecularly hydrogen-bonded conformer in its monomeric form, was found to adopt a partially intermolecularly hydrogen-bonded conformation upon aggregation in a supersonic jet, but symmetric dimers with two or no intermolecular hydrogen bonds are very competitive. A low-temperature FTIR spectral study of solid HA provided evidence for the existence of an open conformation in its condensed phase. Spectral changes were observed during crystallization of HA. The spectrum of the initially deposited disordered sample resembled the simulated spectra of dimer D_{C2} composed of distorted Cc monomeric units, while in the relaxed ordered crystalline structure the observed IR spectrum was consistent with the presence of Ct units in the crystal. In the crystalline phase, the observed changes in the CH asymmetric stretching region also provided useful information for identification of the preferred conformation assumed by HA molecules in the neat solid phases. Complete evidence about the conformation present in HA crystal was provided by X-ray crystallographic (in situ cryocrystallizaton) data, which revealed that in this phase HA acquires a conformation, Ct, which is completely free from intramolecular hydrogen bonds and nonexistent both in the gas phase and in small clusters of the compound. Periodic charge calculations based on the crystal geometry support these observations on a qualitative basis.

ASSOCIATED CONTENT

Supporting Information. Table S1, presenting Cartesian coordinates of three stable dimer structures. Table S2, presenting input and output coordinates for geometry optimizations for unit cell using CRYSTAL09 software package. Complete ref 36. This material is available free of charge via the Internet at http://pubs.acs.org.

AUTHOR INFORMATION

Corresponding Author
asharma@qui.uc.pt

ACKNOWLEDGMENT

We thank the Portuguese Science Foundation (Projects PTDC/QUI/71203/2006-FCOMP-01-0124-FEDER-007458 and PTDC/QUI/111879/2009), cofunded by QREN-COMPETE-UE, and a bilateral collaborative research project FCT-Portugal/DST-India reference FCT/DST (Proc. no. 441.00 INDIA). A.S. thanks FCT for her Post-Doctoral Grant ref.

SFRH/BPD/31840/2006. M.A.S. thanks the Fonds der Chemischen Industrie and the DFG (project Su 121/2) for financial support. S.K.N. thanks DST, India, for research associateship, and R.P. thanks CSIR, India, for financial support. We thank IISc for the XRD facility, and T.N.G.R. thanks DST for a J. C. Bose fellowship.

REFERENCES

(1) Signorell, R.; Luckhaus, D. *J. Phys. Chem. A* **2002**, *106*, 4855–4867.
(2) Signorell, R.; Kunzmann, M. K.; Suhm, M. A. *Chem. Phys. Lett.* **2000**, *329*, 52–60.
(3) Jetzki, M.; Signorell, R. *J. Chem. Phys.* **2002**, *117*, 8063–8073.
(4) Adler, T. B.; Borho, N.; Reiher, M.; Suhm, M. A. *Angew. Chem., Int. Ed.* **2006**, *45*, 3440–3445.
(5) Borho, N.; Suhm, M. A. *Org. Biomol. Chem.* **2003**, *1*, 4351–4358.
(6) Borho, N.; Suhm, M. A. *Phys. Chem. Chem. Phys.* **2004**, *6*, 2885–2890.
(7) Jetzki, M.; Luckhaus, D.; Signorell, R. *Can. J. Chem.* **2004**, *82*, 915–924.
(8) Jalbout, A. F.; Contreras-Torres, F. F.; Adamowicz, L. *Int. J. Quantum Chem.* **2008**, *108*, 279–288.
(9) Apponi, A. J.; Hoy, J. J.; Halfen, D. T.; Ziurys, L. M.; Brewster, M. A. *Astrophys. J.* **2006**, *652*, 1787–1795.
(10) Wu, Y.; Xie, D.; Xue, Y. *J. Comput. Chem.* **2003**, *24*, 931–938.
(11) Mohacek-Grošev, V. *Spectrochim. Acta, Part A* **2005**, *61*, 477–484.
(12) Sharma, A.; Reva, I.; Fausto, R. *J. Phys. Chem. A* **2008**, *112*, 5935–5946.
(13) Cossi, M.; Scalmani, G.; Rega, N.; Barone, V. *J. Chem. Phys.* **2002**, *117*, 43–54.
(14) Cossi, M.; Rega, N.; Scalmani, G.; Barone, V. *J. Comput. Chem.* **2003**, *24*, 669–681.
(15) Zielke, P.; Suhm, M. A. *Phys. Chem. Chem. Phys.* **2006**, *8*, 2826–2830.
(16) Scharge, T.; Wassermann, T. N.; Suhm, M. A. *Z. Phys. Chem.* **2008**, *222*, 1407–1452.
(17) Lucena, Jr., J. R.; Sharma, A.; Reva, I. D.; Araújo, R. M. C. U.; Ventura, E.; do Monte, S. A.; Braga, C. F.; Ramos, M. N.; Fausto, R. *J. Phys. Chem. A* **2008**, *112*, 11641–11648.
(18) Borba, A.; Albrecht, M.; Gómez-Zavaglia, A.; Lapinski, L.; Nowak, M. J.; Suhm, M. A.; Fausto, R. *Phys. Chem. Chem. Phys.* **2008**, *10*, 7010–7021.
(19) Borba, A.; Albrecht, M.; Gómez-Zavaglia, A.; Suhm, M. A.; Fausto, R. *J. Phys. Chem. A* **2010**, *114*, 151–161.
(20) Banerjee, S.; Choudhury, A. R.; Guru Row, T. N.; Chaudhuri, S.; Ghosh, A. *Polyhedron* **2007**, *26*, 24–32.
(21) Chopra, D.; Guru Row, T. N.; Arunan, E.; Klein, R. A. *J. Mol. Struct.* **2010**, *964*, 126–133.
(22) Choudhury, A. R.; Islam, K.; Kirchner, M. T.; Mehta, G.; Guru Row, T. N. *J. Am. Chem. Soc.* **2004**, *126*, 12274–12275.
(23) Chopra, D.; Thiruvenkatam, V.; Guru Row, T. N. *Cryst. Growth Des.* **2006**, *6*, 843–845.
(24) Thalladi, V. R.; Boese, R.; Weiss, H. C. *Angew. Chem., Int. Ed.* **2000**, *39*, 918–922.
(25) Thalladi, V. R.; Boese, R.; Weiss, H. C. *J. Am. Chem. Soc.* **2000**, *122*, 1186–1190.
(26) Thalladi, V. R.; Weiss, H. C.; Blaser, D.; Boese, R.; Nangia, A.; Desiraju, G. R. *J. Am. Chem. Soc.* **1998**, *120*, 8702–8710.
(27) *SMART*; Bruker AXS Inc.: Madison, WI, 2004.
(28) Altomare, A.; Cascarano, G.; Giacovazzo, C.; Guagliardi, A. *J. Appl. Crystallogr.* **1993**, *26*, 343–350.
(29) Sheldrick, G. M. *Program for Crystal Structure Refinement*; University of Göttingen: Germany, 1997.
(30) Farrugia, L. J. *J. Appl. Crystallogr.* **1999**, *32*, 837.
(31) Farrugia, L. J. *J. Appl. Crystallogr.* **1997**, *30*, 565.
(32) Burnett, M. N.; Johnson, C. K. Report ORNL-6895; Oak Ridge National Laboratory, 1996.
(33) Macrae, C. F.; Bruno, I. J.; Chisholm, J. A.; Edgington, P. R.; McCabe, P.; Pidcock, E.; Rodriguez-Monge, L.; Taylor, R.; Van de Streek, J.; Wood, P. A. *J. Appl. Crystallogr.* **2008**, *41*, 466–470.
(34) Nardelli, M. *J. Appl. Crystallogr.* **1995**, *28*, 569.
(35) Spek, A. L. *Acta Crystallogr.* **1990**, *A46*, c34.
(36) Frisch, M. J.; et al. *Gaussian 03*, revision C.02; Gaussian, Inc.: Wallingford, CT, 2004.
(37) Becke, A. D. *Phys. Rev. A* **1988**, *38*, 3098–3100.
(38) Lee, C. T.; Yang, W. T.; Parr, R. G. *Phys. Rev. B* **1988**, *37*, 785–789.
(39) Vosko, S. H.; Wilk, L.; Nusair, M. *Can. J. Phys.* **1980**, *58*, 1200–1211.
(40) Head-Gordon, M.; Pople, J. A.; Frisch, M. J. *Chem. Phys. Lett.* **1988**, *153*, 503–506.
(41) Hariharan, P. C.; Pople, J. A. *Theor. Chim. Acta* **1973**, *28*, 213–222.
(42) Frisch, M. J.; Head-Gordon, M.; Pople, J. A. *Chem. Phys. Lett.* **1990**, *166*, 281–289.
(43) Woon, D. E.; Dunning, T. H. *J. Chem. Phys.* **1993**, *98*, 1358–1371.
(44) Kendall, R. A.; Dunning, T. H.; Harrison, R. J. *J. Chem. Phys.* **1992**, *96*, 6796–6806.
(45) Saunders, V. R.; Dovesi, R.; Roetti, C.; Orlando, R.; Wilson, C. M. Z.; Harrison, N. M.; Doll, K.; Civalleri, B.; Bush, I.; D'Arco, P.; Llunell, M. *CRYSTAL09*; University of Torino: Torino, 2009.
(46) Pascale, F.; Zicovich-Wilson, C. M.; Gejo, F. L.; Civalleri, B.; Orlando, R.; Dovesi, R. *J. Comput. Chem.* **2004**, *25*, 888–897.
(47) Zicovich-Wilson, C. M.; Pascale, F.; Roetti, C.; Saunders, V. R.; Orlando, R.; Dovesi, R. *J. Comput. Chem.* **2004**, *25*, 1873–1881.
(48) Sharma, A.; Reva, I.; Fausto, R. *J. Am. Chem. Soc.* **2009**, *131*, 8752–8753.
(49) (a) Galano, A. *J. Phys. Chem. A* **2006**, *110*, 9153–9160. (b) Andrzejewska, A.; Lapinski, L.; Reva, I.; Fausto, R. *Phys. Chem. Chem. Phys.* **2002**, *14*, 3289–3296.
(50) Dillon, T. J.; Horowitz, A.; Hölscher, D.; Crowley, J. N.; Vereecken, L.; Peeters, J. *Phys. Chem. Chem. Phys.* **2006**, *8*, 236–246.
(51) Hesse, S.; Suhm, M. A. *Phys. Chem. Chem. Phys.* **2009**, *11*, 11157–11170.
(52) Borho, N.; Suhm, M. A.; Le Barbu-Debus, K.; Zehnacker, A. *Phys. Chem. Chem. Phys.* **2006**, *8*, 4449–4460.
(53) Fárník, M.; Weimann, M.; Steinbach, C.; Buck, U.; Borho, N.; Adler, T. B.; Suhm, M. A. *Phys. Chem. Chem. Phys.* **2006**, *8*, 1148–1158.
(54) Scharge, T.; Luckhaus, D.; Suhm, M. A. *Chem. Phys.* **2008**, *346*, 167–175.
(55) Larsen, R. W.; Zielke, P.; Suhm, M. A. *J. Chem. Phys.* **2007**, *126*, 194307.
(56) MacPhail, R. A.; Snyder, R. G.; Strauss, H. L. *J. Chem. Phys.* **1982**, *77*, 1118–1137.
(57) MacPhail, R. A.; Snyder, R. G.; Strauss, H. L. *J. Am. Chem. Soc.* **1980**, *102*, 3976–3976.
(58) Redfield, A. G. *Adv. Magn. Reson.* **1965**, *1*, 1–32.
(59) Wangsness, R. K.; Bloch, F. *Phys. Rev.* **1953**, *89*, 728–739.
(60) Bloch, F. *Phys. Rev.* **1956**, *102*, 104–135.
(61) Wertheimer, R.; Silbey, R. *J. Chem. Phys.* **1981**, *74*, 686–702.
(62) Herzberg, G. *Electronic Spectra and Electronic Structure of Polyatomic Molecules*; Van Nostrand: Princeton, NJ, 1966; p 646.
(63) Kattija-Ari, M.; Harmony, M. D. *Int. J. Quantum Chem.* **1980**, *17*, 443–453.
(64) Bernstein, J.; Davis, R. E.; Shimoni, L.; Chang, N. L. *Angew. Chem., Int. Ed. Engl.* **1995**, *34*, 1555–1573.